



Article

Turbulence Characteristics in the Mixing Layer of a Submerged Cavitating Jet at High Reynolds Numbers

Yongfei Yang ^{1,*} , Gaowei Wang ¹, Weidong Shi ^{1,*}, Wei Li ² , Leilei Ji ² and Hongliang Wang ³¹ School of Mechanical Engineering, Nantong University, Nantong 226019, China² Research Center of Fluid Machinery Engineering and Technology, Jiangsu University, Zhenjiang 212013, China³ School of Aeronautical and Mechanical Engineering, Changzhou Institute of Technology, Changzhou 213032, China

* Correspondence: yyf2020@ntu.edu.cn (Y.Y.); wdshi@ujs.edu.cn (W.S.)

Abstract: In this paper, unsteady and time-averaged turbulence characteristics in a submerged cavitating jet with a high Reynolds number are studied using large eddy simulation. The simulation is validated by comparing the vapor distribution using CFD and a high-speed photography experiment. The results indicate that the currently used numerical method can predict the evolution of the cavitation cloud in the jet accurately. The instantaneous and time-averaged flow fields of the submerged jet with three different cavitation numbers are studied. Comparing the frequency spectral of jets with different cavitation numbers, it is found that, for a fixed location, the frequency increases with the decrease in the cavitation number. Comparing the vorticity distribution at different streamwise locations, the instability process of the ring-shapes vortexes is revealed. Comparing the shape of the cavitation cloud and the vortexes in the jet finds that their spatial distribution and the temporal evolution are similar, indicating that the dynamic characteristics of the vortex and the cavitation affect each other. For the currently investigated cavitating jets, the Reynolds number increases with the decrease in the cavitation number. However, the spreading rate is lower for the jet with higher Reynolds numbers here. This is means that the momentum exchange between the jet and submerging water is reduced by the cavitation phenomenon.

Keywords: cavitating jet; LES; mixing layer; vortex

Citation: Yang, Y.; Wang, G.; Shi, W.; Li, W.; Ji, L.; Wang, H. Turbulence Characteristics in the Mixing Layer of a Submerged Cavitating Jet at High Reynolds Numbers. *Sustainability* **2022**, *14*, 11963. <https://doi.org/10.3390/su141911963>

Academic Editors: Yuquan Zhang, Jianhua Zhang, Ling Zhou and Bin Huang

Received: 16 August 2022

Accepted: 19 September 2022

Published: 22 September 2022

Publisher's Note: MDPI stays neutral with regard to jurisdictional claims in published maps and institutional affiliations.



Copyright: © 2022 by the authors. Licensee MDPI, Basel, Switzerland. This article is an open access article distributed under the terms and conditions of the Creative Commons Attribution (CC BY) license (<https://creativecommons.org/licenses/by/4.0/>).

1. Introduction

In recent years, water jet technology has been widely used in various industrial fields, and water jets injected into pure water environments are called submerged jets. Cavitation is one of the main features of submerged jets, which is a phase change phenomenon that reduces the liquid pressure to the local saturated vapor pressure and transforms the liquid phase into a gas phase [1–3]. The high temperature and pressure generated at the moment of cavitation bubble collapse can cause serious damage to metallic components in hydraulic machinery, but the cavitation bubbles generated by high-pressure water jets can be used for surface strengthening of metallic materials under appropriate conditions [4,5]. The cavitation behavior in submerged jets involves complex and variable physical phenomena, such as turbulence, high temperature and pressure, and phase changes. Therefore, a comprehensive understanding of the turbulence characteristics and cavitation properties of submerged jets is necessary to provide a theoretical basis for the in-depth application of water jet technology.

The current research on submerged jets is mainly based on both experimental studies and numerical simulations. In recent years, many scholars have carried out related works, mainly using High Speed Photography (HSP) to observe the cavitation phenomenon in the jet and Particle Image Velocimetry (PIV) to measure the jet flow field. Zhang Y et al. filled the gap in the literature by experimentally visualizing the internal effects of waves and

turbulence in the wake of a tidal turbine. In order to achieve this, it is crucial to quantify the average wake and turbulence properties, based on the turbine power and wave properties such as the wave energy and its height. Contour plots of velocity deficit, turbulence intensity and wake anisotropy are given for different flow positions [6–8]. Keiichi Sato et al. conducted a high-speed photographic study of a cavitation jet from a contraction–expansion nozzle and obtained the low-frequency and high-frequency signals of vacuolar cluster shedding by the statistics of the cavity length with time, and also captured the diffusion collapse of the vacuolar cloud as it impinges on the material surface using a high-speed photographic camera from the vertical direction [9,10]. Yang Y et al. captured the non-constant flow characteristics of high-pressure cavitation jets at three different angles with HSP experiments, and extracted information on their growth, shedding and collapse from the high-speed images. Finally, the optimal distance and impact performance of cavitation jet reinforcement were investigated [11,12]. Nakano et al. observed the evolution of vacuoles near the submerged jet nozzle using HSP and found that, in the early stage, most of the vacuoles were within the starting vortex and connected to each other in a vortex ring. The vacuoles within the vacuole ring grew rapidly near the nozzle and then gradually decreased in size. In the later stages of jet development, individual vacuoles formed, either connected together or randomly distributed in the jet shear layer [13]. PIV technology is widely used for flow field measurements because of its non-contact measurement properties and its ability to capture transient flow field information with high accuracy. Toshihiro Sawamura et al. performed velocity measurements of the cavitation of the submerged jet using PIV to obtain the average velocity distribution in the region where cavitation exists and found that, in the average velocity distribution, the center of the jet is higher than the edge and the higher region occurs in a part of the edge [14]. Shridhar et al. tested the cavitation vacuoles within the near-flow field of the jet using PIV; they found that the cavitation appeared first in the vortex ring and predicted the probability of cavitation vacuole formation by the distribution pattern, intensity and strain of the cavitation gas nuclei, and the predicted values were in good agreement with the experimental results [15]. Gopalan et al. studied the cavitation phenomenon in submerged water jets using PIV, and the PIV observations showed that the cavitation bubbles were mainly generated at the center of the vortex in turbulent flows [16]. Mao N et al. used Time-resolved Particle Image Velocimetry (TR-PIV) to measure the submerged jet flow field and orthogonal decomposition (POD) to extract the large-scale energy-containing vortex structure, and the results show that, as the pump pressure increases, shearing between the jet edge and ambient water increases, entrainment of the surrounding fluid is enhanced, and the cavitation cloud profile fluctuates dramatically under high-pressure conditions [17].

Since high-pressure submerged water jets are usually accompanied by cavitation, and the concentration of vacuoles increases when the cavitation number of the jet is low, it is difficult to accurately measure the internal flow field by means of visual measurements such as PIV; therefore, it is important to develop numerical simulation techniques for high-pressure submerged water jets. Martin M et al. conducted numerical simulations and experimental studies for submerged rotating jets, and various RANS models were used to calculate the flow field to obtain the velocity distribution at different locations of the jet [18]. Yang Y used three different turbulence models to represent the RANS and RANS-LES hybrid models and compared the probabilities of these models to simulate microscale vortex structures. By analyzing the relationship between small-scale vortices and cavitation formation, the probability of these models to simulate strong shear stress high-pressure cavitation jets is discussed [19,20]. Thus, LES is a feasible method to simulate the jet flow field. Yong Wang et al. used large eddy simulation to simulate the heat transfer process of the impinging jet and obtained the accurate heat transfer process of the jet cooling device by numerical calculation; they proposed a numerical simulation-based design method for the jet cooling device [21]. Y. C. Wang et al. used large eddy simulation combined with the Schnerr–Sauer cavitation model to study the high-Reynolds-number three-dimensional flow structure of a submerged jet in an axisymmetric cavity. The computational results

capture the transient vortex structure and the three-dimensional flow structure in the shear layer. The growth of the jet's shear layer is not linearly diffused by the impactor [22,23].

In this paper, unsteady and time-averaged turbulence characteristics in a submerged cavitating jet with high Reynolds numbers are studied using large eddy simulation. The simulation is validated by comparing the vapor distribution using CFD and a high-speed photography experiment. Both instantaneous and time-averaged flow fields of the submerged jet with three different cavitation numbers are studied.

2. Experiment and CFD Method

2.1. Experiment Apparatus and Method

The unsteady characteristics and velocity field of the jet are tested using high-speed photography and particle image velocimetry (PIV). The experimental apparatus is shown in Figure 1. The pressure of the system is supplied by a plunger pump. The rated pressure is 50 MPa, and the rated flow rate is 15 L/min. The main part of the test bench is composed of upper and lower water tanks, and the upper tank is made of transparent material polymethyl methacrylate. During the experiment, the upstream pressure of the nozzle can be changed by controlling the rotating speed of the pump. For the high-speed photography, an Olympus Ispeed Camera is used to capture the image of the cavitation cloud, with a frequency of 20,000 fps. Under this frame rate, images with a pixel size of 352×272 can be obtained, which are finally analyzed by image-processing algorithms in MATLAB.

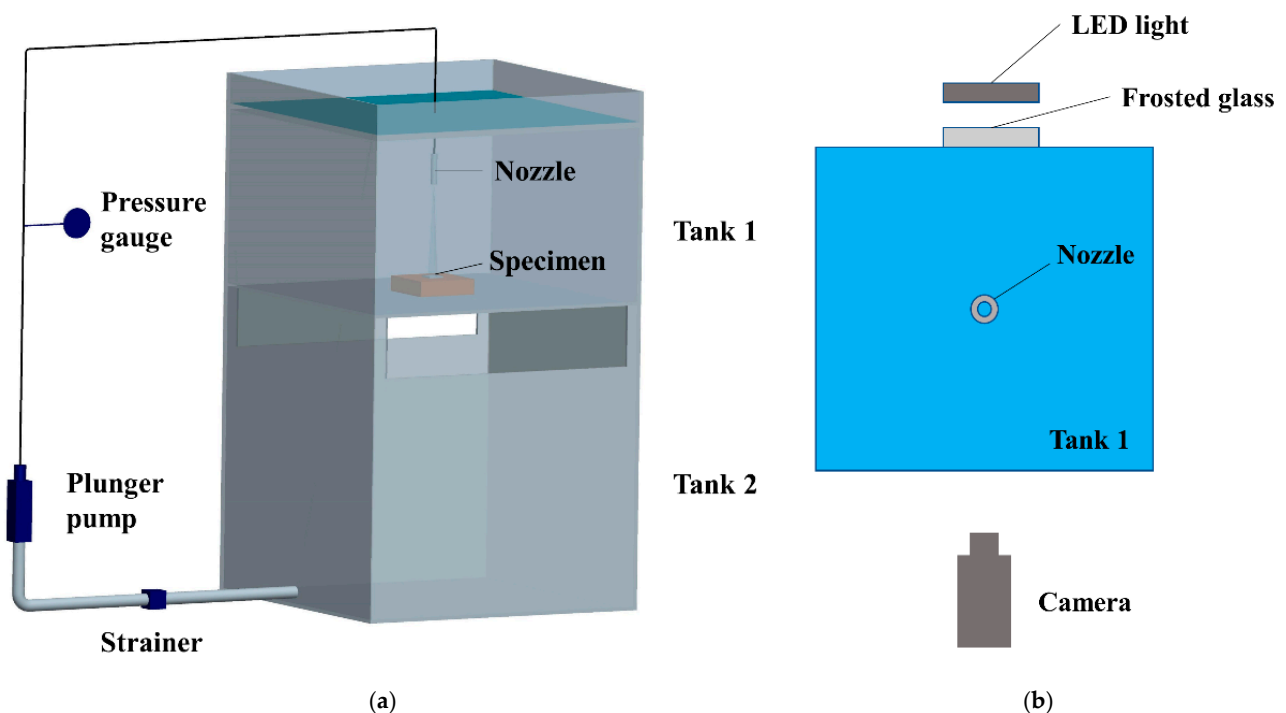


Figure 1. Experimental apparatus for cavitation jet. (a) High-pressure jet system; (b) High-speed photography.

2.2. Governing Equations and LES Approach

To reveal the structure of the vortex and the velocity fluctuations in the shear layer, the LES approach is used for the simulation of the submerged cavitating jet under high Reynolds numbers. Continuity and momentum equations are used as the governing equations, and the mixture model is used for the mixed-phase flow field calculation, and its control equations are as follows [24]:

$$\frac{\partial \rho}{\partial t} + \frac{\partial (\rho \bar{u}_j)}{\partial x_j} = 0 \quad (1)$$

$$\frac{\partial(\rho\bar{u}_j)}{\partial t} + \frac{\partial(\rho\bar{u}_i\bar{u}_j)}{\partial x_j} = -\frac{\partial\bar{p}}{\partial x_i} + \frac{\partial}{\partial x_i} \left(\mu \frac{\partial\bar{u}_i}{\partial x_i} \right) - \frac{\partial\tau_{ij}}{\partial x_j} \quad (2)$$

where u_i is the velocity component in direction i , p is the pressure for both vapor and liquid phases, and ρ and μ denote the mixture density and viscosity, respectively, which are defined as follows:

$$\rho = \sum_{k=1}^n \alpha_k \rho_k \quad (3)$$

$$\mu = \sum_{k=1}^n \alpha_k \mu_k \quad (4)$$

In Equation (2), τ_{ij} represents the subgrid-scale stresses (SGS), which are defined as follows:

$$\tau_{ij} = \rho(\bar{u}_i\bar{u}_j - \bar{u}_i\bar{u}_j) \quad (5)$$

After the filtering operation, the SGS are unknown and need modeling. The current simulation is solved using Fluent and the subgrid-scale turbulence models employ the Boussinesq hypothesis. The subgrid-scale turbulent stresses are calculated as follows [25]:

$$\tau_{ij} - \frac{1}{3}\tau_{kk}\delta_{ij} = -2\mu_t\bar{S}_{ij} \quad (6)$$

where \bar{S}_{ij} is the tensor of the rate of strain for the resolved scale, which is defined as:

$$\bar{S}_{ij} = \frac{1}{2} \left(\frac{\partial\bar{u}_i}{\partial x_j} + \frac{\partial\bar{u}_j}{\partial x_i} \right) \quad (7)$$

In Equation (7), μ_t is the subgrid-scale turbulence viscosity and it is closed by the wall-adapting local eddy viscosity (WALE) model in this simulation. In the WALE model, the subgrid-scale turbulence viscosity is modeled as follows:

$$\mu_t = \rho L_s^2 \frac{\left(S_{ij}^d S_{ij}^d \right)^{3/2}}{\left(\bar{S}_{ij} \bar{S}_{ij} \right)^{5/2} + \left(S_{ij}^d S_{ij}^d \right)^{5/4}} \quad (8)$$

where L_s and S_{ij}^d in the WALE model are defined as:

$$L_s = \min(kd, C_w V^{1/3}) \quad (9)$$

$$S_{ij}^d = \frac{1}{2} \left(\bar{g}_{ij}^2 + \bar{g}_{ji}^2 \right) - \frac{1}{3} \delta_{ij} \bar{g}_{kk}^2, \quad \bar{g}_{ij} = \frac{\partial\bar{u}_i}{\partial x_j} \quad (10)$$

where k is the von Kármán constant and C_w is the default WALE constant set as the default value 0.325.

2.3. Physical Cavitation Model

When the cavitation phenomenon is considered in the simulation, the transport function of the vapor volume fraction is used [26]:

$$\frac{\partial}{\partial t} (\alpha \rho_v) + \nabla \cdot (\alpha \rho_v \vec{v}_v) = R_e - R_c \quad (11)$$

where α is the volume fraction of the vapor and R_e and R_c represent the vaporization and condensation rate, respectively, which can be obtained from the cavitation model.

Currently, different cavitation models are deduced by researchers and most of them are based on the Rayleigh–Plesset function. In this paper, the Zwart–Gerber–Belamri model

is used to calculate the mass transfer between the vapor and the liquid phases. The mass transfer equation of the cavitation model is shown as follows:

$$R_e = F_{\text{vap}} \frac{3\alpha_{\text{nuc}}(1 - \alpha_v)\rho_v}{R_B} \sqrt{\frac{2}{3} \frac{P_v - P}{\rho_l}} \text{ when } P \leq P_v \quad (12)$$

$$R_c = F_{\text{cond}} \frac{3\alpha_v\rho_v}{R_B} \sqrt{\frac{2}{3} \frac{P - P_v}{\rho_l}} \text{ when } P > P_v \quad (13)$$

where R_B is the radius of the homogenous bubbles, α_{nuc} is the volume fraction of non-condensable gas, F_{vap} is the vaporization rate coefficient, and F_{cond} is the condensation rate coefficient.

2.4. Simulation Setup

The simulation domain and conditions are set according to the experiment. A nozzle with a throat diameter of 2 mm is simulated, and the fluid domain with enough size is created to avoid the influence of the boundaries on the jet flow. As shown in Figure 2, the calculation domain has a diameter of $100d$ and a length of $250d$. The present analysis is focused on the turbulence characteristics of the shear layer, which is located in the region of the outlet of the nozzle. The fluid domain is discretized into hexahedral grids using ANSYS ICEM, as shown in Figure 2. Since the focus is on a deep understanding of the flow in the mixing layer, the mesh in the shear layer closed to the nozzle outlet is refined. The total grid cell number for the whole domain is 39 million.

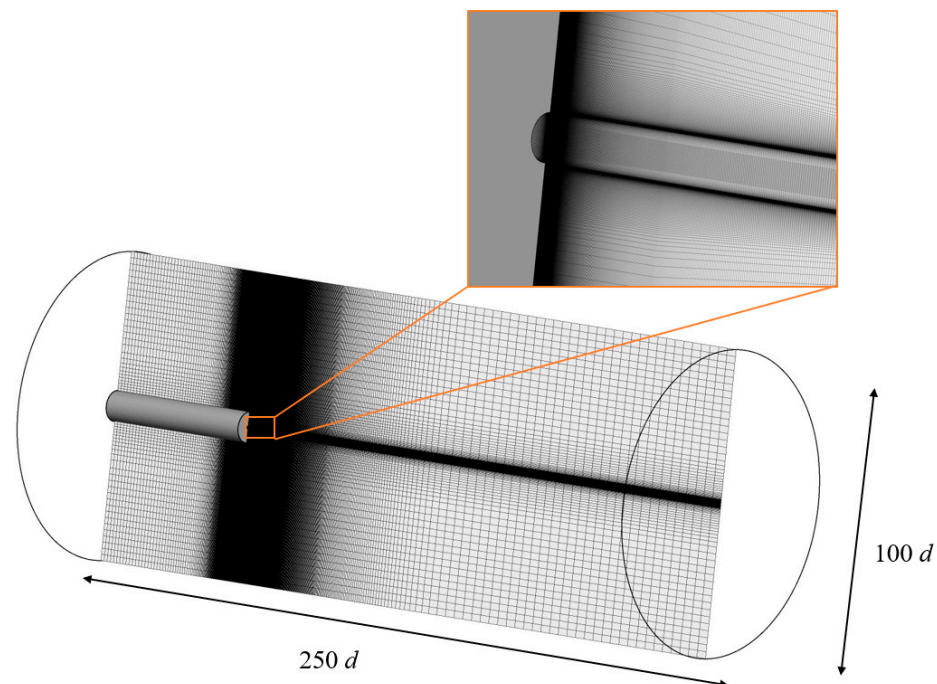


Figure 2. Mesh and sizes of the computational domain.

The numerical simulation contains three main types of boundary conditions. At the upstream inlet of the nozzle, the boundary is set as the pressure inlet, and the total pressure is set as 1–3 MPa, regarding the working conditions of the jet. The outlet of the domain is treated as the pressure outlet, and the gauge pressure is set as 0 Pa. The other boundaries are set as the wall. The time step is $100 \mu\text{s}$ and the residuals for the continuity equation, and the momentum and volume fraction transport equations, are 10^{-3} . The maximum iteration number for each time step is set as 30. The transient simulation was calculated for 1000 time steps initially, and then the velocity and pressure at the monitored point were stored for

1000 more time steps. Physical parameters in the whole domain were averaged for the last 1000 time steps to obtain the time-averaged value for the velocity and pressure fields.

3. Results and Discussion

3.1. Validation of CFD Results

Simulation of the cavitating jet is carried out according to the experiment, and the three working conditions of the jet are investigated both numerically and experimentally. Figure 3 shows the comparison between the high-speed image and the simulation results. Cavitation performance of a submerged jet is mainly affected by the nozzle geometry and the working conditions of the jet. The commonly used parameter to describe the working conditions is cavitation number, which is defined as follows:

$$\sigma = \frac{p_c - P_v}{\frac{1}{2}\rho v^2} \quad (14)$$

where p_c is the pressure at the downstream of the nozzle, P_v is the vapor pressure of the fluid, ρ is the density and v is the jet velocity. For the jet with a high value of p_c , the cavitation number can be defined approximately as:

$$\sigma = \frac{p_c}{\varphi \Delta p} \approx \frac{p_c}{\Delta p} \quad (15)$$

where φ is the flow coefficient, which is usually in the range of 0.97 to 0.98, and Δp is the pressure difference between the upstream and downstream sides of the nozzle throat.

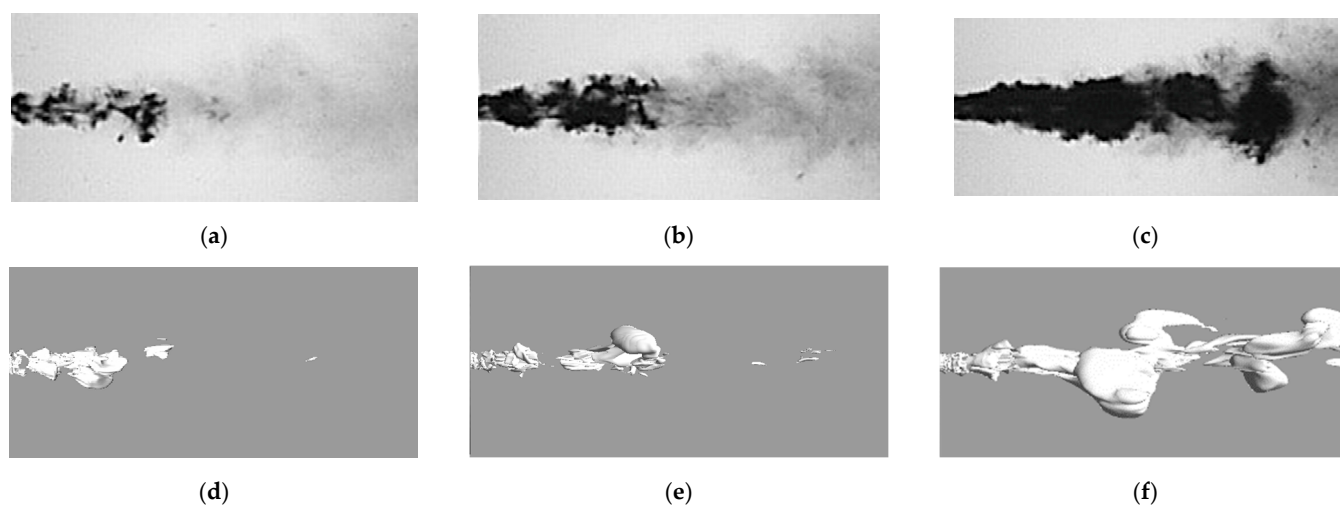


Figure 3. Cavitation cloud distribution by experiment and numerical prediction. (a) Exp. ($\sigma = 0.1$); (b) Exp. ($\sigma = 0.05$); (c) Exp. ($\sigma = 0.033$); (d) CFD ($\sigma = 0.1$); (e) CFD ($\sigma = 0.05$); (f) CFD ($\sigma = 0.033$).

Figure 3 shows the experiment results of the high-speed photography and the LES simulation of the jet for three different cavitation numbers, namely, $\sigma = 0.1$, 0.05 and 0.033. The images show that the length of the cavitation clouds increases obviously with the decrease in the cavitation number. When the cavitation number is 0.1, the cavitation bubbles only appear around the nozzle exit, while the bubble cloud length is almost doubled for the case when the cavitation number is 0.033. Figure 3d–f is the iso-surface of the vapor phase in the simulation result. By comparing the experimental and simulated results, it is found that the tendency and the scale of the cavitation cloud for CFD and high-speed photography are almost the same.

The time-averaged images of the high-speed images and the simulation results are compared in Figure 4. As shown in the images, gray-scale values of 5000 high-speed images are averaged, which represent the volume fraction of the vapor phase. For the simulation

results, volume fraction values of more than 1000 time steps are calculated statistically, which is shown in Figure 4d–f. By comparing the time-averaged value of the cavitation cloud from experimental images and numerical simulation, it is found that the length of the jet is basically the same. The scale of the jet for both radial and axial directions are similar for experimental and numerical results. The results indicate that the currently used numerical method can predict the evolution of the cavitation cloud in the jet accurately.

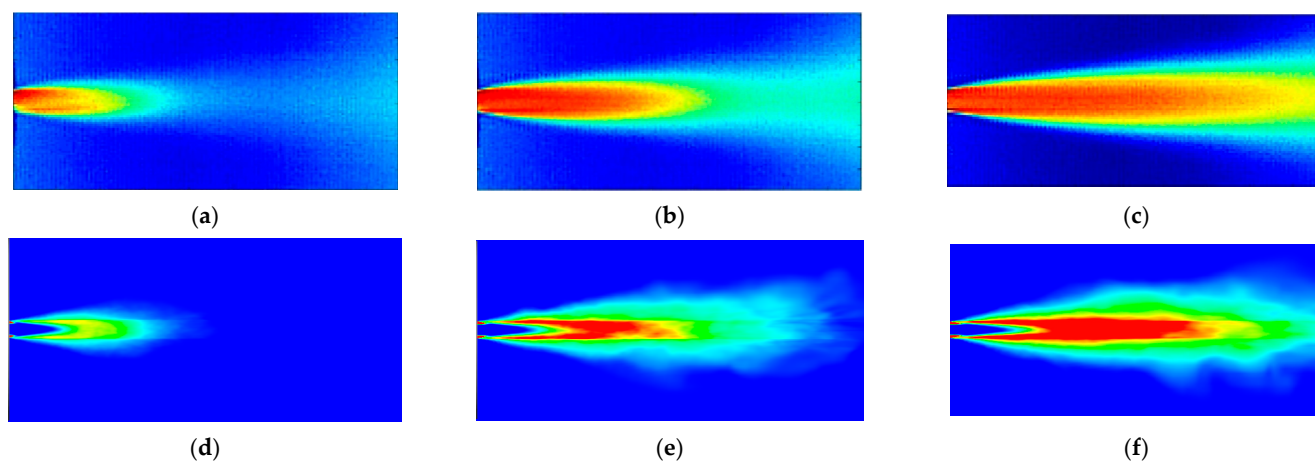


Figure 4. Time-averaged results of the cavitation clouds. (a) Exp. ($\sigma = 0.1$); (b) Exp. ($\sigma = 0.05$); (c) Exp. ($\sigma = 0.033$); (d) CFD ($\sigma = 0.1$); (e) CFD ($\sigma = 0.05$); (f) CFD ($\sigma = 0.033$).

3.2. Shear Layer Instability

When the high-speed jet is submerged in the relatively stationary fluid, velocity changes from hundreds of meters per second to zero in a small range of distance spatially in the radial direction. Under such conditions, the high-momentum fluid is affected by the surrounding fluid with low momentum by viscous forces. Figure 5 shows the transient velocity field of the submerged high-pressure jet in the region close to the nozzle exit, and the related cavitation number is $\sigma = 0.05$. It can be seen that the velocity decreases fast along the streamwise direction, and the velocity in the mixing layer fluctuates dramatically. At the same time, vortical structures can be found in the mixing layer, and the spatial scale of the vortices increases gradually along the axial direction. This tendency is in accordance with the characteristic of shear layer Kelvin–Helmholtz instability [27]. The Kelvin–Helmholtz instability is a flow instability that arises due to shear stress along the interface between two different fluids and results in a concentration of vorticity along a velocity discontinuity in the tangent line.

To show the vortex structures in the mixing layer more clearly, the plane streamline in the mixing layer near the nozzle exit is plotted, which is colored by the velocity magnitude. Vortices in the mixing layer can be seen clearly in Figure 6. Small-scale vortices started to appear at the boundary layer of the nozzle throat outlet, which is mainly caused by the counter flow between the streamwise main flow and the reversed flow from the region close to the end wall of the nozzle exit. The small-scale vortices grow gradually, since the surrounding stationary fluid is entrained by the main flow. Meanwhile, the vortices merge with each other in the early stages of the evolution and then break into small-scale vortices under the effect of pressure and velocity fluctuations caused by the turbulence. Since the cavitation performance of the submerged high-pressure jet depends on the vortices in the shear layer, it is of great importance to investigate the structure of the vortices and the turbulence characteristics in the mixing layer. To observe the location of the vortices and the spatial distribution of the velocity magnitude, it can be found that the velocity gradient in the mixing layer is not smooth, and each wave of the fluctuation corresponds to a large-scale vortex. In certain regions downstream of the nozzle exit, the wavelength of the velocity fluctuation increases, and the scale of the vortex increases in the same tendency.

This indicates that the velocity fluctuation can be caused by the interaction and evolution of the vortices in the mixing layer under the high shear stress between the high-speed and stationary fluid.

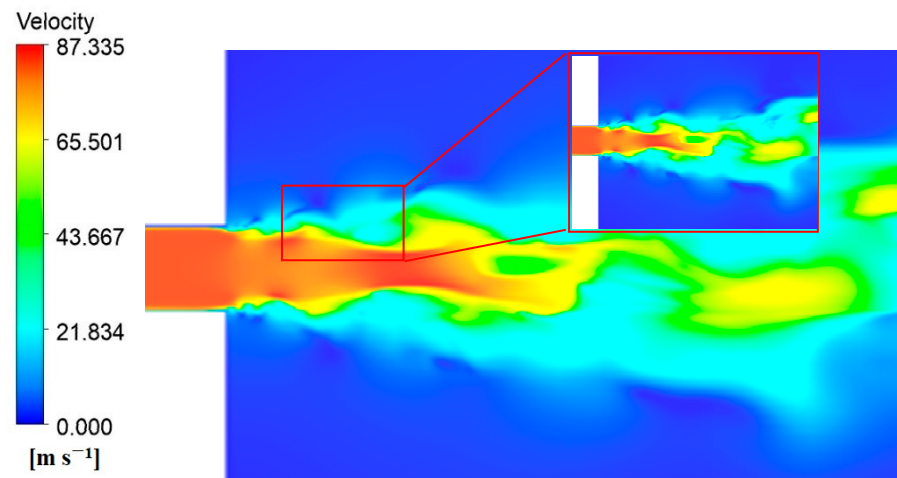


Figure 5. Velocity distribution of submerged cavitation jet ($\sigma = 0.05$).

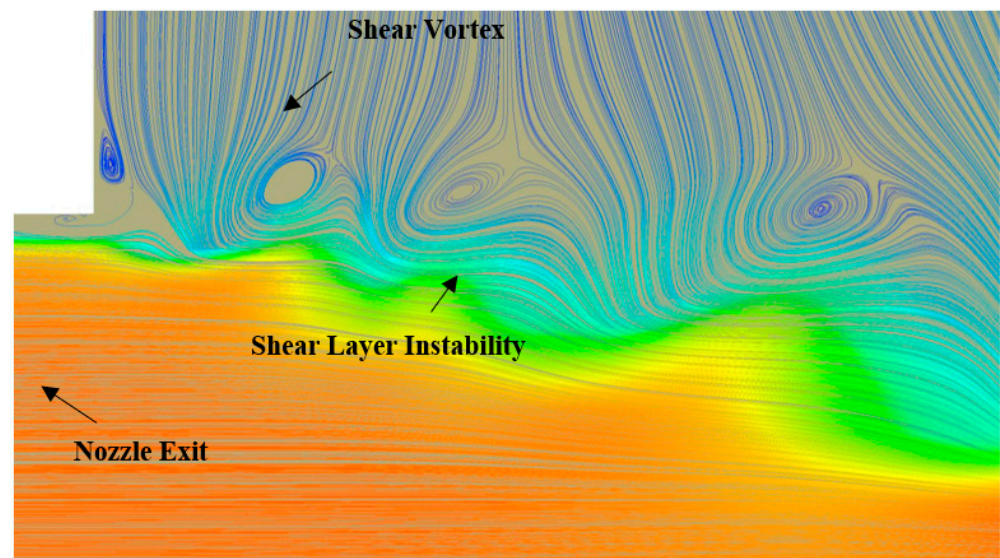


Figure 6. Shear layer instability in the submerged high-pressure jet ($\sigma = 0.05$).

According to the findings, the cavitating jet always sheds in a certain frequency, particularly in the case of self-excited oscillating cavitating jets. The exiting frequency and the theory play an important role in the design of the nozzle for the self-excited oscillating jet. To reveal the unsteady characteristic of the jet, streamwise velocity variations at different locations are monitored. The monitor points are located along the center line of the jet, from the nozzle exit to $10d$ downstream. Figure 7 shows the time domain variation of the axial component of the velocity for three different cavitation numbers. It can be seen from the figures that the variation amplitude of the velocity increases obviously along the streamwise direction for each cavitation number. It indicates that the turbulence structures and the intensity are smaller in the region close to the nozzle, which increases gradually as the vortices merge with each other and diffuse during motion. Comparing the monitored signals for the three different cavitation numbers, it can be seen that the velocity increases with the decrease in the cavitation number, since the pressure difference between the nozzle throat is increased. At the point $x/d = 2$, the variation of the velocity is relatively small for the three cavitation numbers, which means that the instability structures here are relatively

small. Comparing the transient velocity at $x/d = 2.5$, it can be found that high-amplitude velocity fluctuations occur in the case with a high cavitation number, while the velocity variation still remains low in the case with lower cavitation numbers. When the cavitation number is $\sigma = 0.1$, at the point $x/d = 2.5$, the velocity varies from 20 m/s to 50 m/s, and the profile of the axial velocity in the time domain is similar to that at the further downstream point $x/d = 3$. This means that the turbulence is fully developed at the position $x/d = 2.5$, and the vortex structures become isotropic from this point. When the cavitation number is decreased to $\sigma = 0.05$, the transient axial velocity at $x/d = 2.5$ only shows several peaks, indicating large-scale and intensive instability starts to happen at this position. When $\sigma = 0.033$, the instability happens further downstream, where $x/d = 3$.

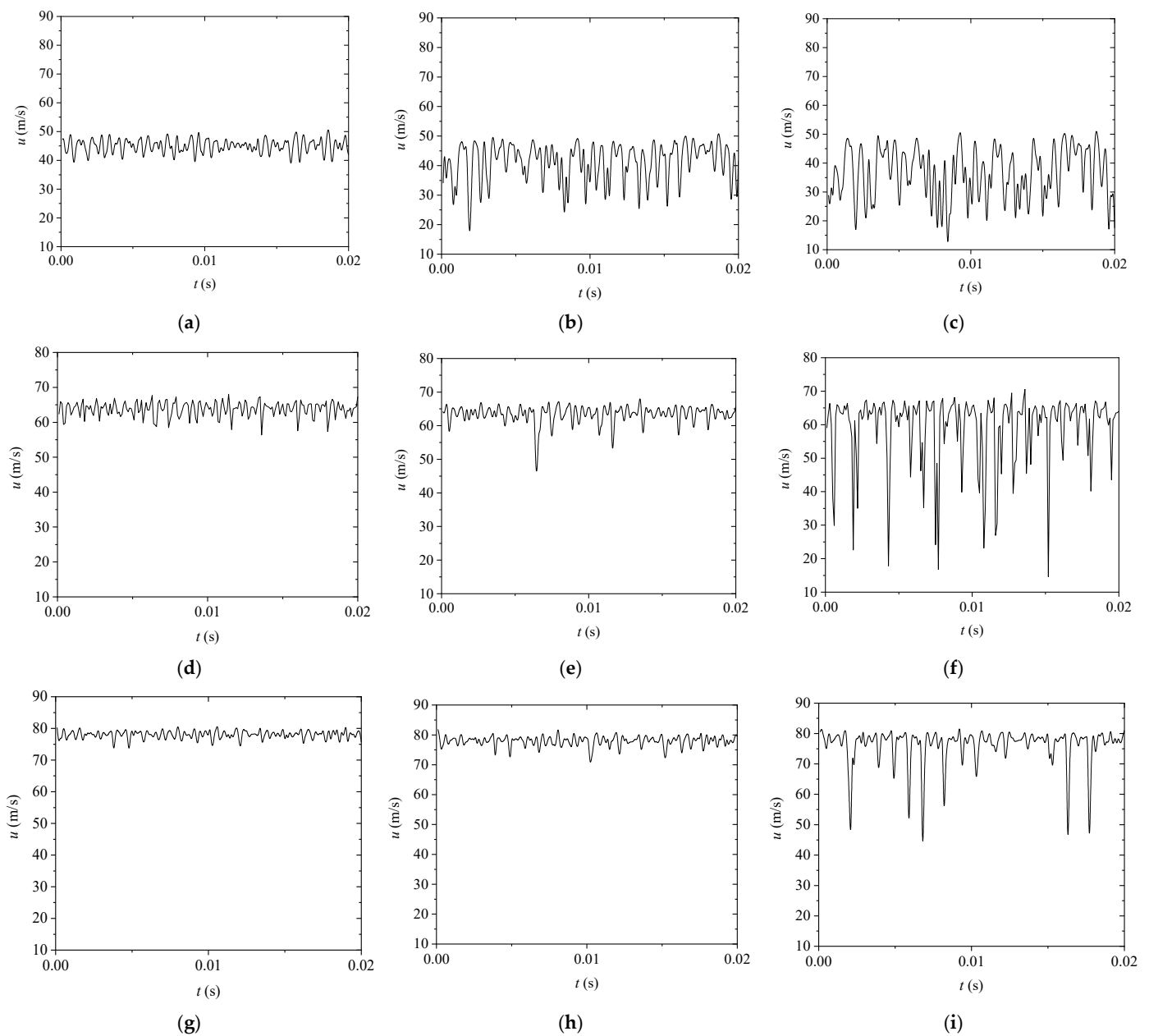


Figure 7. x-component velocity signals and the corresponding spectra inside the mixing layer. (a) $\sigma = 0.1$, $x/d = 2$; (b) $\sigma = 0.1$, $x/d = 2.5$; (c) $\sigma = 0.1$, $x/d = 3$; (d) $\sigma = 0.05$, $x/d = 2$; (e) $\sigma = 0.05$, $x/d = 2.5$; (f) $\sigma = 0.05$, $x/d = 3$; (g) $\sigma = 0.033$, $x/d = 2$; (h) $\sigma = 0.033$, $x/d = 2.5$; (i) $\sigma = 0.033$, $x/d = 3$.

To analyze the frequency characteristic of the turbulence flow in the cavitating jet, the monitored transient streamwise velocity was transformed to frequency field by FFT. Figure 8 shows the frequency of the temporal signal of the velocity component along the center line for different cavitation numbers. It can be seen from the figures that the main frequency of the velocity oscillation decreases as the monitor point moves downstream. The oscillation of the streamwise velocity reflects the vortex structures in the flow field. The scale of the vortices increases and has a momentum exchange with the surrounding fluid in the process while moving downstream, which causes the decrease in the main frequency of the velocity magnitude. Comparing the frequency spectral of jets with different cavitation numbers, it can be found that, for a fixed location, the frequency increases with the decrease in the cavitation number. This is because, in the case of low cavitation numbers, the pressure differences between the inlet and outlet of the nozzle are larger, which produces jets with higher initial velocity. The jet with higher initial velocity contains more momentum, which decreases more slowly.

3.3. Vortexes and Cavitation in the Mixing Layer

As discussed above, the velocity in the jet varies in the complicated mode with the effect of the turbulence. It contains both low- and high-frequency signals, which may be caused by different types of vortexes with different size. To reveal the temporal evolution of the vortex structure in the mixing layer, vortexes near the nozzle outlet around one period are plotted. Figure 9 shows the Q-criterion iso-surface for the jet with a cavitation number of $\sigma = 0.05$, which is colored by the velocity magnitude. At the time when $t = 0$ s, the vortex in the fluid close to the nozzle is relatively weak and almost no vortex structure can be found in the nozzle. At $t = 60$ μ s, a vortex ring is formed at the nozzle outlet. Spanwise vortexes dominate in the region $x/d = 0$ to 1.5, while a streamwise vortex shows up at around $x/d = 2$. The vortex dissipates gradually further downstream under the effect of the viscous force. At $t = 120$ μ s, the newly formed vortex ring is broken into small-scale vortexes under the strong shear stress, and the streamwise vortex mostly disappears. After that, the region with strong vortexes is reduced, and the next period starts at around $t = 300$ μ s. From the frequency distribution of the temporal spectral of the velocity, a wide band signal can be found. This can be related to the formation, distortion and breakage of the vortex ring structures.

To discuss the formation of the instability of the vortex ring, the vorticity magnitude on the plane perpendicular to the axis at different positions is displayed in Figure 10. It can be seen from the figures that, at the position just behind the nozzle outlet, the vortex is distributed in a circular region. The shape of the region with a high vorticity value is more regular in the case with a lower cavitation number, indicating that higher jet velocity makes the ring vortexes more stable. The same tendency can be observed on the plane at $x/d = 1.5$ and 3 for different cavitation numbers. Comparing the vorticity distribution at different streamwise locations, the instability process of the ring-shaped vortexes is revealed. Under the effect of the viscous force of the fluid, the second instability happens on the ring-shaped vortexes. The vortex ring breaks into several parts while moving downstream, due to the entrainment of the low-momentum fluid. The streamwise vortex structures show up accompanying the second instability of the vortex ring. In addition, it can be seen from the figure that the jet is affected by the shear vortex at the nozzle outlet to form a small vortex band, and the vortex gradually grows with the diffusion of the jet and is accompanied by dissipation.

Cavitation always happens in a high-pressure submerged jet when the jet velocity is high enough. The theory of the shear-induced Rankin vortex model can be used to explain the appearance of cavitation in the jet, and the vortex–bubble interaction is found to have an effect on the fluid and bubble dynamics to some degree. Figure 11 shows the iso-surface of the vapor volume fraction, from which the dynamic behavior of the cavitation cloud is reflected. From the figures, it is found that the vapor is mainly formed at the nozzle outlet. This is in accordance with the Rankin vortex theory. When the high-speed jet flows out from

the nozzle, the high shear stress is formed in the mixing layer and a series of small-scale vortices develops due to the K–H instability. The pressure in the Rankin vortex center decreases fast and reaches the vapor pressure of the fluid under the ambient temperature, and the cavitation occurs at the same time. A ring-shaped cavitation cloud is found at the nozzle outlet at the time $t = 60 \mu\text{s}$, and a vortex ring is created at the same location at the same time, according to Figure 11b. Then, the ring-shaped cavitation breaks into small parts under the effect of the vortex instability. Comparing the shape of the cavitation cloud and the vortices in the jet, it is found that their spatial distribution and the temporal evolution are similar, indicating that the dynamic characteristics of the vortex and the cavitation affect each other.

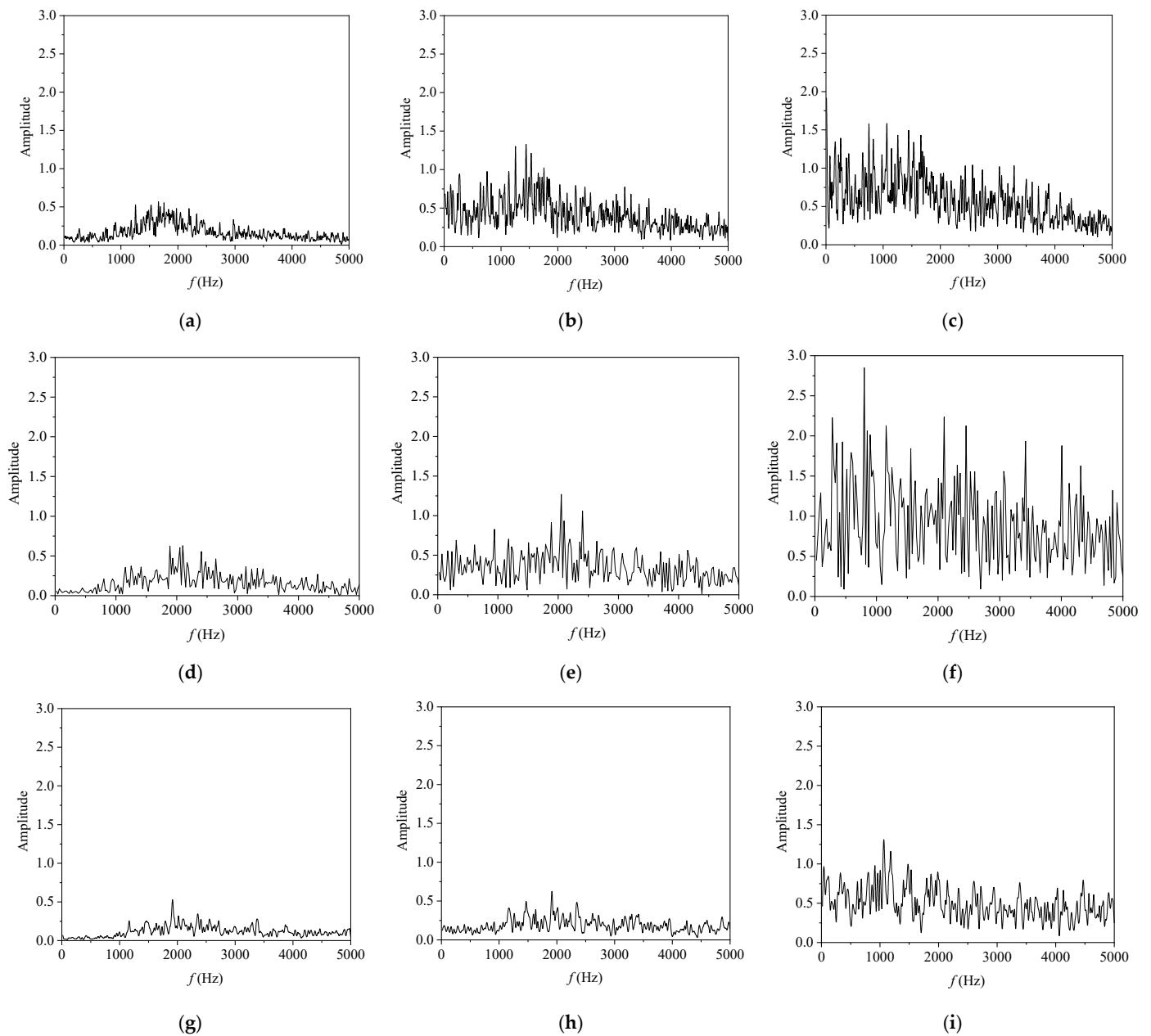


Figure 8. The frequency of the temporal signal of the velocity component along the center line. (a) $\sigma = 0.1$, $x/d = 2$; (b) $\sigma = 0.1$, $x/d = 2.5$; (c) $\sigma = 0.1$, $x/d = 3$; (d) $\sigma = 0.05$, $x/d = 2$; (e) $\sigma = 0.05$, $x/d = 2.5$; (f) $\sigma = 0.05$, $x/d = 3$; (g) $\sigma = 0.033$, $x/d = 2$; (h) $\sigma = 0.033$, $x/d = 2.5$; (i) $\sigma = 0.033$, $x/d = 3$.

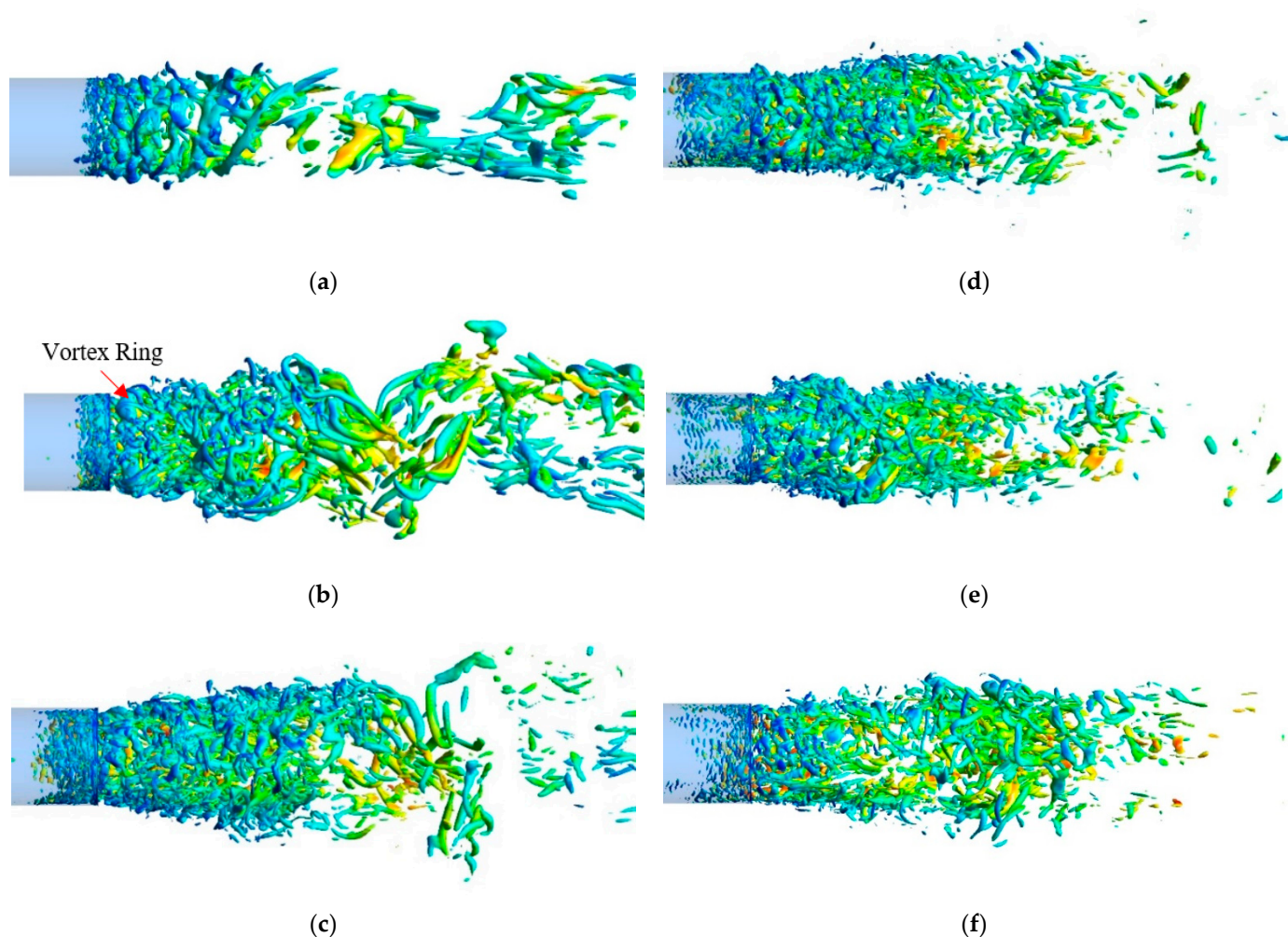


Figure 9. Vortex structure and evolution in the mixing layer ($\sigma = 0.05$). (a) $t = 0$ s; (b) $t = 60 \mu\text{s}$; (c) $t = 120 \mu\text{s}$; (d) $t = 180 \mu\text{s}$; (e) $t = 240 \mu\text{s}$; (f) $t = 300 \mu\text{s}$.

3.4. Time-Averaged Characteristics

To analyze the time-averaged characteristics of the jet, 1000 time steps of the transient simulation were averaged and statistically processed. Figure 12 shows the axial velocity along the center line and the radial direction at different x/D locations. As shown in Figure 12a, the velocity remains almost unchanged for a distance in the region close to the nozzle outlet, which is called the core region of the jet. It is found that the core region of the jet is extended as the cavitation number is decreased, since the momentum and the initial velocity are higher for the condition with a lower cavitation number. According to the research literature about submerged jets without cavitation, the velocity profile of the jet along the jet axis shows a similarity law, and the profile changes little when the Reynolds number is changed [28]. In the current research, the submerged jets are cavitating jets, and the variation of the non-dimensional velocity profile changes with the variation of the cavitation number. One reason for this change is the difference of the vapor volume fraction. It is well known that the density and the viscosity of the vapor phase is obviously lower than that of the liquid phase, and the appearance of the cavitation may reduce the moment exchange between the high-speed jet and the surrounding fluids. Figure 12b presents the velocity distribution along the radial direction at different x/D locations, from which the jet's spreading rate can be compared. Trushar B. Gohil et al. [29] concluded that the radial variation shows a top-hat profile at the location close to the nozzle exit, and this profile is changed gradually at the downstream locations; the spreading rate is higher for the case with a high Reynolds number. In the current cavitating jets, a top-hat profile is

also found. For the currently investigated cavitating jets, the Reynolds number increases with the decrease in the cavitation number. However, the spreading rate is lower for the jet with a higher Reynolds number here. This means that the momentum exchange between the jet and submerging water is reduced by the cavitation phenomenon.

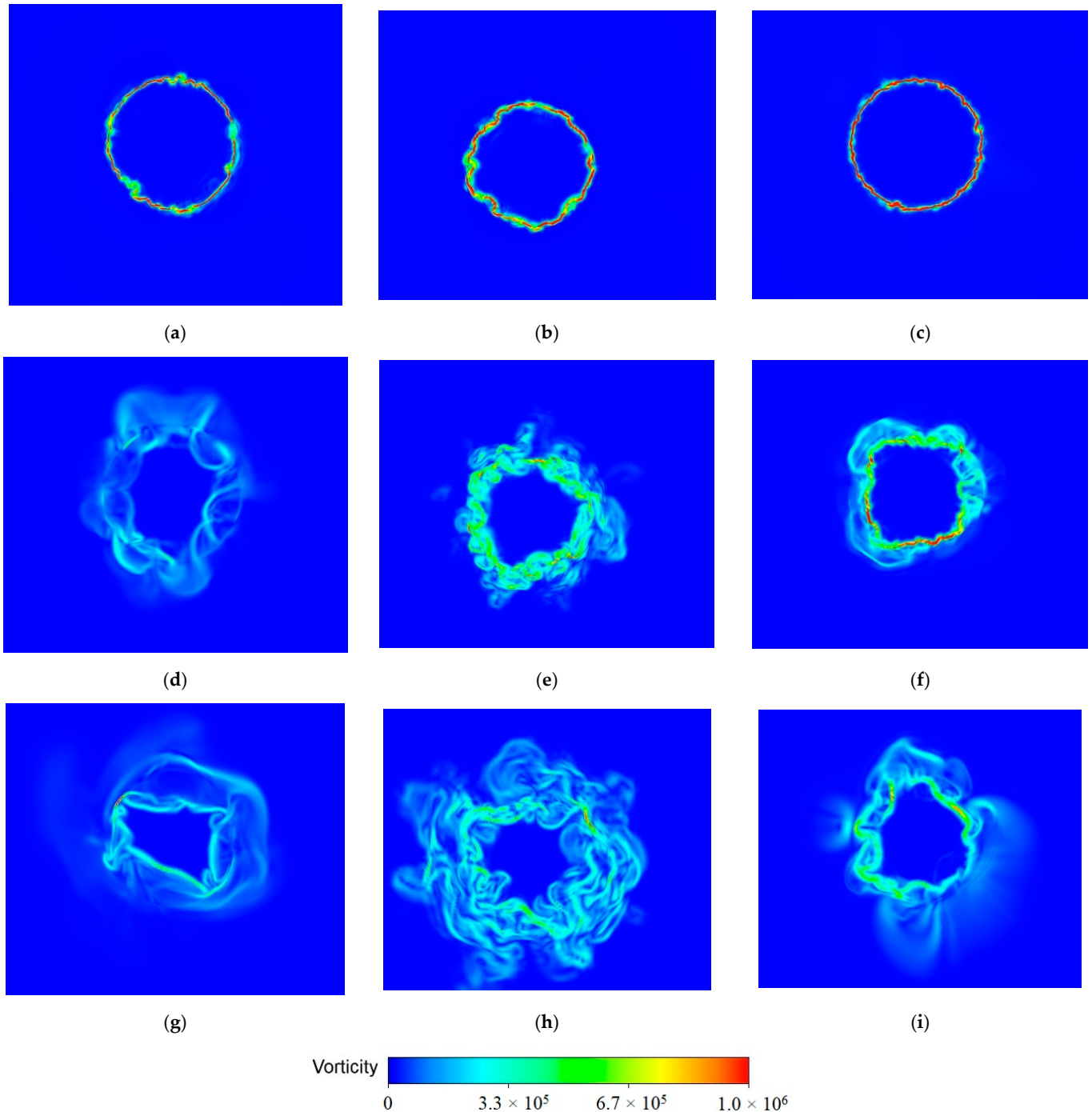


Figure 10. Contour shape of the vorticity on the cross-section at different streamwise locations. (a) $\sigma = 0.1$, $x/d = 0.05$; (b) $\sigma = 0.05$, $x/d = 0.05$; (c) $\sigma = 0.033$, $x/d = 0.05$; (d) $\sigma = 0.1$, $x/d = 1.5$; (e) $\sigma = 0.05$, $x/d = 1.5$; (f) $\sigma = 0.033$, $x/d = 1.5$; (g) $\sigma = 0.1$, $x/d = 3$; (h) $\sigma = 0.05$, $x/d = 3$; (i) $\sigma = 0.033$, $x/d = 3$.

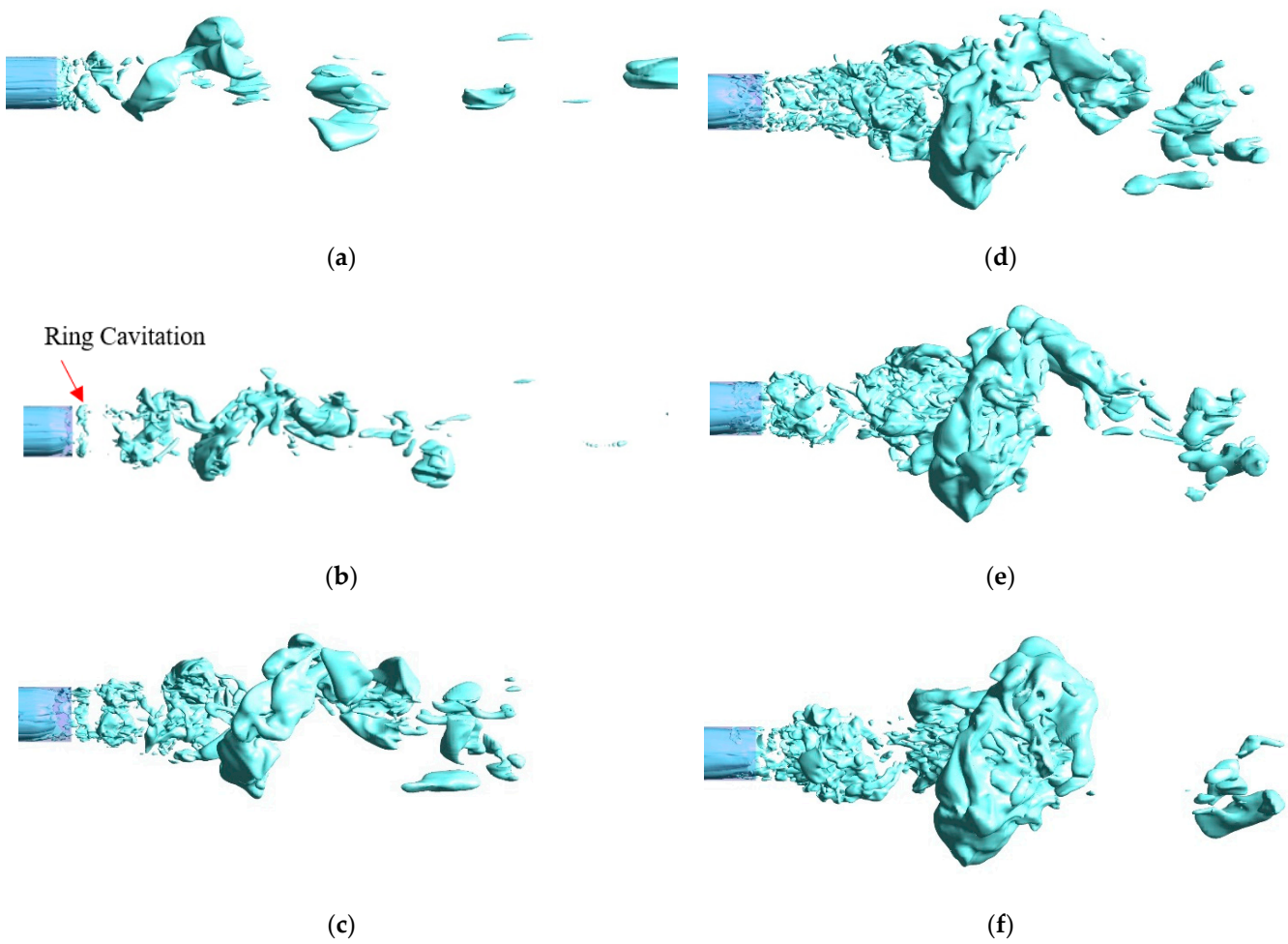


Figure 11. Cavitation evolution near the shear layer of the jet ($\sigma = 0.05$). (a) $t = 0$ s; (b) $t = 60$ μ s; (c) $t = 120$ μ s; (d) $t = 180$ μ s; (e) $t = 240$ μ s; (f) $t = 300$ μ s.

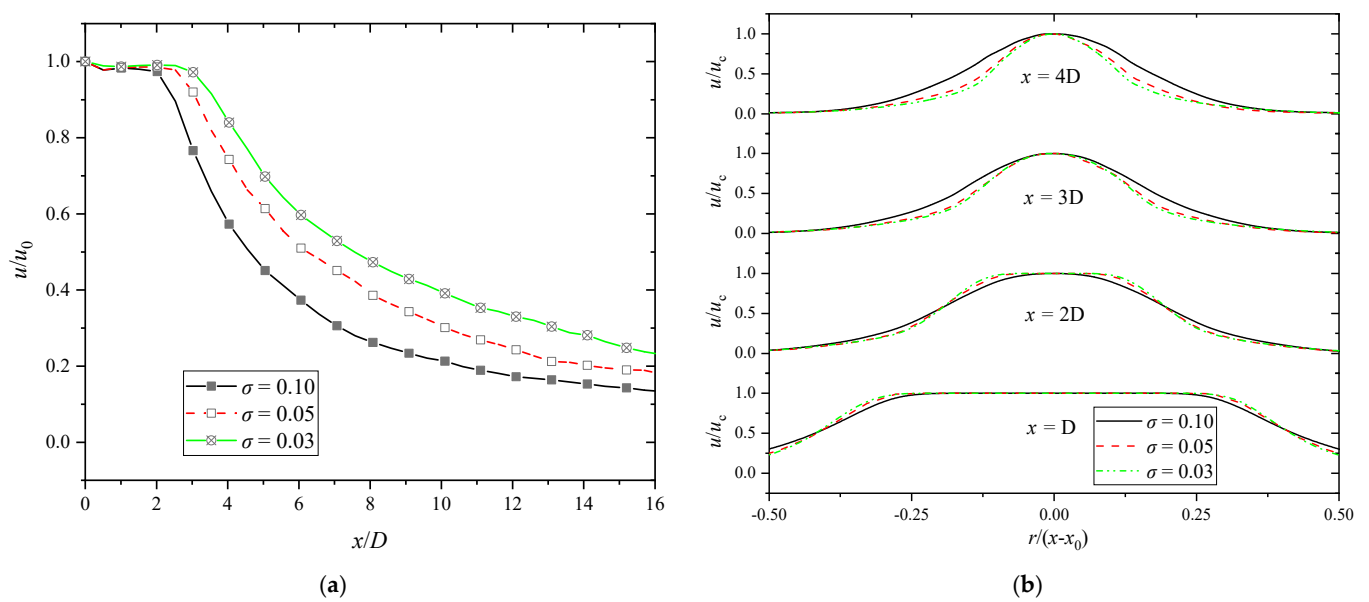


Figure 12. Axial velocity along the center line and radial direction at different x/D locations. (a) Streamwise variation; (b) Radial variation.

According to the research about jets, the spreading rate can be quantitatively analyzed using the jet's half-width and mixing layer thickness. The definition of the jet half-width is the radial length where the axial velocity decreases to half of the center value. For a typical shear flow, the mixing layer is defined as follows [30]:

$$\delta_w = \frac{\bar{u}_1 - \bar{u}_2}{(\partial \bar{u} / \partial y)_{max}} \quad (16)$$

where \bar{u}_1 and \bar{u}_2 are time-averaged streamwise velocities at different sides of the shear layer. Figure 13 illustrates the shear layer thickness and half-width variation along the streamwise direction of the jet. The mixing layer thickness and the half-width increases slightly within the potential core for all three cavitation numbers, and then increases fast further downstream. In general, the mixing layer and half-width of the jet are larger for the case with a higher cavitation number. Since the jet velocity and the Reynolds number are higher in the case with a low cavitation number, the variation of the mixing layer along the streamwise direction is different from that of research on non-cavitating jets [29]. This indicates that the occurrence of the cavitation has a great effect on the momentum exchange in the mixing layer.

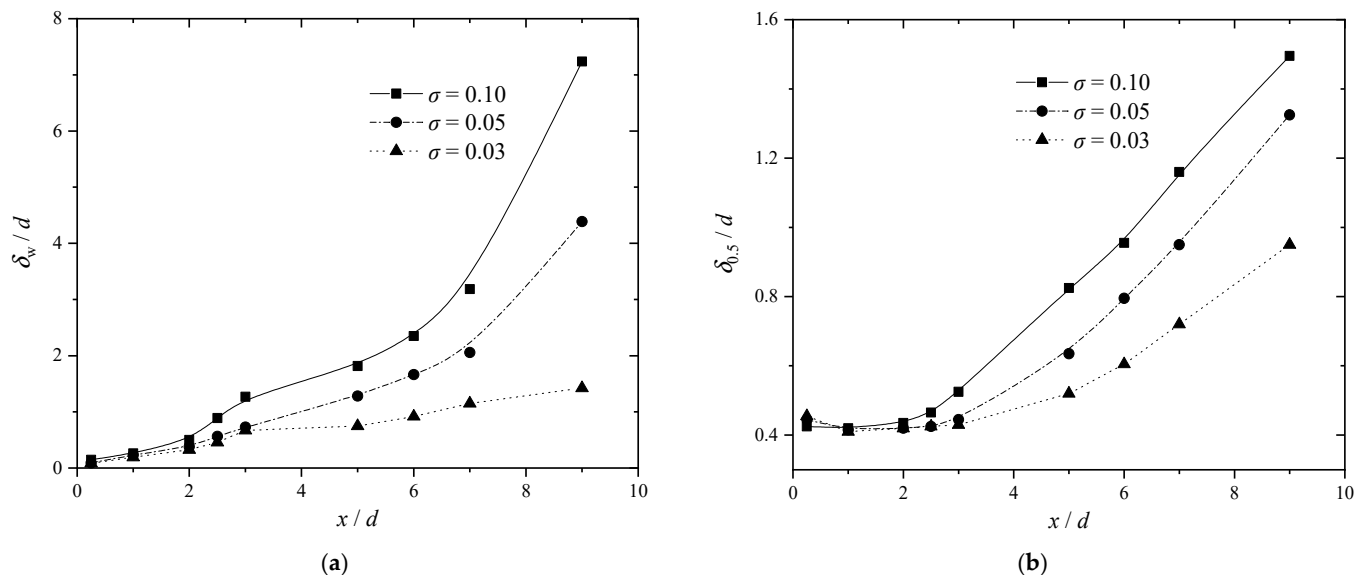


Figure 13. Variation of shear layer thickness and half-width variation along the streamwise direction. (a) Shear layer thickness; (b) Half-width variation.

4. Conclusions

The length of the cavitation clouds increases obviously with the decrease in the cavitation number; the scale of the jet for both radial and axial direction is similar for experimental and numerical results. The currently used numerical method can predict the evolution of the cavitation cloud in the jet accurately. The turbulence structures and the intensity are smaller in the region close to the nozzle, which increases gradually as the vortices merge with each other and diffuse during motion. Comparing the monitored signals for the three different cavitation numbers, it can be seen that the velocity increases with the decrease in the cavitation number, since the pressure difference between the nozzle throat is increased. Under the effect of the viscous force of the fluid, the second instability happens on the ring-shaped vortices. The vortex ring breaks into several parts while moving downstream, due to the entrainment of the low-momentum fluid. The streamwise vortex structures show up accompanying the second instability of the vortex ring. The core region of the jet is extended as the cavitation number is decreased, since the momentum and the initial velocity are higher for the condition with a lower cavitation

number. The spreading rate is lower for the jet with a higher Reynolds number. This means that the momentum exchange between the jet and submerging water is reduced by the cavitation phenomenon.

Author Contributions: Data curation, W.S. and L.J.; Methodology, L.J.; Project administration, W.S.; Resources, W.S. and H.W.; Software, G.W.; Supervision, H.W.; Visualization, W.L.; Writing—original draft, Y.Y. and G.W.; Writing—review and editing, Y.Y. All authors have read and agreed to the published version of the manuscript.

Funding: This research was funded by the National Key Research and Development Project of China (No. 2019YFB 2005300), National High-Tech Ship Scientific Research Project of China (No. MIIT [2019] 360), National Natural Science Foundation of China (No. 51979138), National Natural Science Foundation of China (No. 273746), National Natural Science Foundation of China (No. 51979240), Jiangsu Natural Science Re-search Project (No. 19KJB470029), China Postdoctoral Science Foundation (No. 273746), and Natural Science Foundation of Jiangsu Province (No. BK20220609), Project funded by China Postdoctoral Science Foundation (No.2022TQ0127).

Institutional Review Board Statement: Not applicable.

Informed Consent Statement: Not applicable.

Data Availability Statement: Data on the analysis and reporting results during the study can be obtained by contacting the authors.

Conflicts of Interest: The authors declare no conflict of interest.

References

1. Soyama, H. Cavitating Jet: A Review. *Appl. Sci.* **2020**, *10*, 7280. [[CrossRef](#)]
2. Vasilakis, E.S.; Kyriazis, N.; Koukouvinis, P.; Farhat, M.; Gavaises, M. Cavitation induction by projectile impacting on a water jet. *Int. J. Multiph. Flow* **2019**, *114*, 128–139. [[CrossRef](#)]
3. Ijiri, M.; Shimonishi, D.; Nakagawa, D.; Yoshimura, T. New water jet cavitation technology to increase number and size of cavitation bubbles and its effect on pure Al surface. *Int. J. Lightwght Mater. Manuf.* **2018**, *1*, 12–20. [[CrossRef](#)]
4. Soyama, H. Cavitation Peening: A Review. *Metals* **2020**, *10*, 270. [[CrossRef](#)]
5. Soyama, H.; Takeo, F. Comparison between cavitation peening and shot peening for extending the fatigue life of a duralumin plate with a hole. *J. Mater. Process. Technol.* **2016**, *227*, 80–87. [[CrossRef](#)]
6. Zhang, Y.; Zang, W.; Zheng, J.; Cappiotti, L.; Zhang, J.; Zheng, Y.; Fernandez-Rodriguez, E. The influence of waves propagating with the current on the wake of a tidal stream turbine. *Appl. Energy* **2021**, *290*, 116729. [[CrossRef](#)]
7. Zhang, Y.; Zhang, J.; Lin, X.; Wang, R.; Zhang, C.; Zhao, J. Experimental investigation into downstream field of a horizontal axis tidal stream turbine supported by a mono pile. *Appl. Ocean. Res.* **2020**, *101*, 102257. [[CrossRef](#)]
8. Zhang, Y.; Zhang, Z.; Zheng, J.; Zhang, J.; Zheng, Y.; Zang, W.; Lin, X.; Fernandez-Rodriguez, E. Experimental investigation into effects of boundary proximity and blockage on horizontal-axis tidal turbine wake. *Ocean. Eng.* **2021**, *225*, 108829. [[CrossRef](#)]
9. Saito, Y.; Sato, K. Instantaneous Behavior of Cavitation Clouds at Impingement of Cavitating Water-Jet. *Prog. Multiph. Flow Res.* **2007**, *2007*, 47–53. [[CrossRef](#)]
10. Sato, K.; Sugimoto, Y.; Ohjimi, S. *Pressure-Wave Formation and Collapses of Cavitation Clouds Impinging on Solid Wall in a Submerged Water Jet*; University of Michigan: Ann Arbor, MI, USA, 2011.
11. Yang, Y.; Li, W.; Shi, W.; Wang, C.; Zhang, W. Experimental Study on Submerged High-Pressure Jet and Parameter Optimization for Cavitation Peening. *Mechanika* **2020**, *26*, 346–353. [[CrossRef](#)]
12. Zhang, W.; Ma, N.; Ma, J.; Li, C.; Ren, J. Experimental Study on the Unsteady Characteristics and the Impact Performance of a High-Pressure Submerged Cavitation Jet. *Shock. Vib.* **2020**, *2020*, 8862849.
13. Nakano, K.; Hayakawa, M.; Fujikawa, S.; Yano, T. Cavitation Bubbles in a Starting Submerged Water Jet. *Nihon Kikai Gakkai Ronbunshu B Hen Trans. Jpn. Soc. Mech. Eng. Part B* **2001**, *69*, 5. [[CrossRef](#)]
14. Sawamura, T.; Koshika, N. Velocity Measurement of Cavitation in Cavitating Jet Flow. *Proc. JSME Annu. Meet.* **2003**, *2003*, 155–156. [[CrossRef](#)]
15. Gopalan, S.; Katz, J.; Knio, O. Near-field flow structure and cavitation inception in jets. In Proceedings of the 3rd ASME-JSME Joint Fluids Engineering Conference, San Francisco, CA, USA, 18–23 July 1999.
16. Gopalan, S.; Katz, J.; Knio, O. The flow structure in the near field of jets and its effect on cavitation inception. *J. Fluid Mech.* **1999**, *398*, 1–43. [[CrossRef](#)]
17. Mao, N.; Kang, C.; Zhou, M.M. POD Analysis of Submerged Jet Structure and Cavitation Cloud Evolution. *J. Eng. Thermophys.* **2019**, *40*, 2036–2042.
18. Miltner, M.; Jordan, C.; Harasek, M. CFD simulation of straight and slightly swirling turbulent free jets using different RANS-turbulence models. *Appl. Therm. Eng.* **2015**, *89*, 1117–1126. [[CrossRef](#)]

19. Yang, Y.; Shi, W.; Tan, L.; Li, W.; Chen, S.; Pan, B. Numerical Research of the Submerged High-Pressure Cavitation Water Jet Based on the RANS-LES Hybrid Model. *Shock. Vib.* **2021**, *2021*, 6616718. [[CrossRef](#)]
20. Yang, Y.; Li, W.; Shi, W.; Zhang, W.; El-Emam, M.A. Numerical Investigation of a High-Pressure Submerged Jet Using a Cavitation Model Considering Effects of Shear Stress. *Processes* **2019**, *7*, 541. [[CrossRef](#)]
21. Wang, Y.; Yuan, G.; Yoon, Y.-K.; Allen, M.G.; Bidstrup, S.A. Large eddy simulation (LES) for synthetic jet thermal management. *Int. J. Heat Mass Transf.* **2006**, *49*, 2173–2179. [[CrossRef](#)]
22. Wang, Y.C.; Tan, L.; Cao, S.L.; Gao, C.C. Numerical study on flow structures of high Reynolds number submerged jet in an axis-symmetric cavity. In Proceedings of the 2014 ISFMFE-6th International Symposium on Fluid Machinery and Fluid Engineering, Wuhan, China, 22 October 2014.
23. Wang, Y.C.; Gao, C.C.; Tan, L.; Cao, S.L. Hysteresis properties of submerged jet cavitation in axis-symmetrical cavity. *J. Vib. Shock.* **2015**, *34*, 118–122.
24. Manninen, M.; Taivassalo, V.; Kallio, S. *Mixture Model for Multiphase Flow*; U.S. Department of Energy, Office of Scientific and Technical Information (OSTI): Oak Ridge, TN, USA, 1996.
25. Nicoud, F.; Ducros, F. Subgrid-Scale Stress Modelling Based on the Square of the Velocity Gradient Tensor. *Flow Turbul. Combust.* **1999**, *62*, 183–200. [[CrossRef](#)]
26. Zwart, P.J.; Gerber, A.G.; Belamri, T. A two-phase flow model for predicting cavitation dynamics. In Proceedings of the 5th International Conference on Multiphase Flow, Yokohama, Japan, 30 May–4 June 2004.
27. Friedlander, S.; Lipton-Lifschitz, A. Chapter 8 Localized Instabilities in Fluids. *Handb. Math. Fluid Dyn.* **2003**, *2*, 289–354.
28. Gohil, T.B.; Saha, A.K.; Muralidhar, K. Large eddy simulation of a free circular jet. *J. Fluids Eng.* **2014**, *136*, 051205. [[CrossRef](#)]
29. Gohil, T.B.; Saha, A.K.; Muralidhar, K. Numerical study of instability mechanisms in a circular jet at low Reynolds numbers. *Comput. Fluids* **2012**, *64*, 1–18. [[CrossRef](#)]
30. Brown, G.L.; Roshko, A. On density effects and large structure in turbulent mixing layers. *J. Fluid Mech. Digit. Arch.* **1974**, *64*, 775–816. [[CrossRef](#)]